



# Core–shell structured reduced graphene oxide wrapped magnetically separable rGO@CuZnO@Fe<sub>3</sub>O<sub>4</sub> microspheres as superior photocatalyst for CO<sub>2</sub> reduction under visible light

Pawan Kumar <sup>a</sup>, Chetan Joshi <sup>a</sup>, Alexandre Barras <sup>b</sup>, Brigitte Sieber <sup>c</sup>, Ahmed Addad <sup>c</sup>, Luc Boussekey <sup>d</sup>, Sabine Szunerits <sup>b</sup>, Rabah Boukherroub <sup>b,\*</sup>, Suman L. Jain <sup>a,\*</sup>

<sup>a</sup> Chemical Science Division, CSIR–Indian Institute of Petroleum, Dehradun, 248005, India

<sup>b</sup> Univ. Lille, CNRS, Centrale Lille, ISEN, Univ. Valenciennes, UMR 8520 – IEMN, F-59000 Lille, France

<sup>c</sup> UMET, UMR CNRS 8207, Université Lille 1, 59655 Villeneuve d'Ascq Cédex, France

<sup>d</sup> LASIR, UMR CNRS 8516, Université Lille 1, 59655 Villeneuve d'Ascq Cédex, France



## ARTICLE INFO

### Article history:

Received 14 March 2016

Received in revised form

24 November 2016

Accepted 29 November 2016

Available online 29 November 2016

### Keywords:

Core–shell structure

Iron nanoparticles

Zinc oxide

Reduced graphene oxide

Photocatalysis

Visible light

CO<sub>2</sub> reduction

## ABSTRACT

A highly efficient, recyclable and magnetically separable core–shell structured CuZnO@Fe<sub>3</sub>O<sub>4</sub> microsphere wrapped with reduced graphene oxide (rGO@CuZnO@Fe<sub>3</sub>O<sub>4</sub>) photocatalyst has been developed and used for the photoreduction of carbon dioxide with water to produce methanol under visible light irradiation. Owing to the synergistic effect of the components and to the presence of a thin Fe<sub>2</sub>O<sub>3</sub> layer on Fe<sub>3</sub>O<sub>4</sub>, rGO@CuZnO@Fe<sub>3</sub>O<sub>4</sub> **4** exhibited higher catalytic activity as compared to the other possible combinations such as CuZnO@Fe<sub>3</sub>O<sub>4</sub> **2** and GO@CuZnO@Fe<sub>3</sub>O<sub>4</sub> **3** microspheres. The yield of methanol in case of using **2** and **3** as photocatalyst was found to be 858 and 1749 μmol g<sup>−1</sup> cat, respectively. However, the yield was increased to 2656 μmol g<sup>−1</sup> cat when rGO@CuZnO@Fe<sub>3</sub>O<sub>4</sub> **4** was used as photocatalyst under similar experimental conditions. This superior photocatalytic activity of **4** was assumed to be due to the restoration of the sp<sup>2</sup> hybridized aromatic system in rGO, which facilitated the movement of electrons and resulted in better charge separation. The synthesized heterogeneous photocatalyst could readily be recovered by external magnet and successfully reused for six subsequent cycles without significant loss in the product yield.

© 2016 Published by Elsevier B.V.

## 1. Introduction

The rising demand for fossil fuels resulted in emissions of large quantities of carbon dioxide (CO<sub>2</sub>) in the atmosphere, which has become a severe environmental issue associated with global warming and climate change [1]. Furthermore, the depletion of hydrocarbon fuels is an inevitable problem which has to be faced in the near future. Therefore, conversion of CO<sub>2</sub> into value-added chemicals such as hydrocarbons is of great importance that can help in tackling both environmental as well as energy issues. More importantly, CO<sub>2</sub> conversion into fuel (energy) that not only mitigates CO<sub>2</sub> emissions, but also recycles it back as a fuel feedstock is highly desirable in meeting clean energy demand [2–4].

CO<sub>2</sub> conversion can be achieved through different means based on chemical, electrochemical, biological and photochemi-

cal approaches. Among them, biomimetic artificial photosynthesis has recently gained considerable attention as a promising technology for reduction of CO<sub>2</sub> to fuel using solar energy [4–6]. In this process, the hydrocarbons are produced by photoreduction of CO<sub>2</sub> using water and solar energy. This method has gained considerable importance in recent years as it is economically viable and environmentally friendly. A large variety of semiconductor materials such as TiO<sub>2</sub>, ZnO, ZrO<sub>2</sub>, CdS, Fe<sub>2</sub>O<sub>3</sub>, SiC, WO<sub>3</sub> and transition metal complexes have been extensively investigated for photocatalytic conversion of CO<sub>2</sub> [4,7]. Since redox potentials of large band gap semiconductors are more adapted for CO<sub>2</sub> photoreduction, TiO<sub>2</sub>–based photocatalysts have been widely investigated for this transformation [7,8]. Even though higher yields were obtained with metal complexes as compared to TiO<sub>2</sub> photocatalysts, metal complexes, besides being expensive and unstable under UV light, often required an electron donor (e.g. triethylamine), whereas water molecules were used as electron donor for TiO<sub>2</sub> [8]. Band gap engineering by doping with metals and non metals (Cu, Ag, Ru, N, etc.) was used for improvement of the conversion efficiency, but still

\* Corresponding authors.

E-mail address: [suman@iip.res.in](mailto:suman@iip.res.in) (S.L. Jain).

no satisfactory improvements were achieved [9–12]. Zinc oxide (ZnO), although less investigated than TiO<sub>2</sub> for CO<sub>2</sub> photoreduction, is a wide band gap (3.37 eV) material which can be established as an interesting alternative due to its superior photocatalytic activity, low cost and environmentally friendly properties. In order to extend the operation conditions to higher wavelength, metallic or non metallic elements can be introduced to ZnO material. Yarahmadi and Sharifnia successfully used dye photosensitized ZnO with Co, Ni and Cu phthalocyanines (Pc) for the photocatalytic conversion of CO<sub>2</sub> and CH<sub>4</sub> under visible light [13]. Formation of ZnO/ZnTe cation heterostructure exhibited good photocatalytic activity for the reduction of CO<sub>2</sub> into CH<sub>4</sub> under visible light [14].

Recently, graphene oxide (GO), reduced graphene oxide (rGO) and their nanocomposites have emerged as interesting materials with potential applications in various fields [15–17]. Hsu et al. were the first to report the photocatalytic efficiency of GO for the conversion of CO<sub>2</sub> to methanol under visible light and the conversion rate was found to be 6-fold higher than commonly used TiO<sub>2</sub> photocatalyst [18]. The combination of graphene with semiconductor photocatalysts provided nanocomposites which have shown improved photocatalytic performance for CO<sub>2</sub> photoreduction [19–22]. In these nanocomposites, graphene acted as an efficient electron acceptor to enhance the charge transfer and thus reduces the electron-hole pair recombination in the composite to improve the photocatalytic activity. It has been also demonstrated that in TiO<sub>2</sub>-graphene based nanocomposites, the less defective graphene displayed a significantly larger enhancement in CO<sub>2</sub> photoreduction under visible light irradiation. This effect has been assigned to the superior mobility of charge carriers on graphene sheets, facilitating the diffusion of photoexcited electrons to reactive sites [19]. ZnO-rGO prepared through a simple hydrothermal process showed enhanced photocatalytic activity for the reduction of CO<sub>2</sub> to CH<sub>3</sub>OH. The yield of CH<sub>3</sub>OH on ZnO-rGO was found to be five times higher than that obtained on pure ZnO. The ZnO-rGO nanocomposites possessed excellent cycling property [23]. Similarly, loading copper nanoparticles (Cu NPs) of 4–5 nm in diameter onto GO was found to enhance the photocatalytic performance of pristine GO for the reduction of CO<sub>2</sub> to acetaldehyde and methanol under visible light irradiation [24]. An enhancement factor greater than 60 times has been achieved using Cu NPs/GO compared to pristine GO. The increased photocatalytic activity of GO was attributed to the suppression of electron–hole pair recombination, reduction of GO's band gap and modification of its work function. Independently, An et al. examined the catalytic activity of Cu<sub>2</sub>O microparticles supported on reduced graphene oxide (Cu<sub>2</sub>O/rGO) for the photoreduction of CO<sub>2</sub> [25]. The obtained results clearly demonstrated the positive effect of coupling Cu<sub>2</sub>O with rGO, as witnessed by two times enhancement of the Cu<sub>2</sub>O photoreduction activity and selectivity with CO being the only reduction product. Moreover, incorporation of Cu<sub>2</sub>O onto rGO sheets improved the photocatalyst stability remarkably, holding a great potential for CO<sub>2</sub> conversion in a sustainable manner.

GO and rGO functionalization with visible light absorbing transition metal complexes and clusters was recently adopted as a very effective strategy to enhance the photocatalytic performance of GO (rGO) for the reduction of CO<sub>2</sub> into methanol. Various transition metal complexes such as ruthenium trinuclear polyazine complex [26], cobalt(II) phthalocyanine [27], copper(II) complex [28], heteroleptic ruthenium complex [29] and hexamolybdenum clusters [30] have been anchored to GO or nitrogen-doped graphene and successfully used as effective photocatalysts for the reduction of CO<sub>2</sub> into methanol under visible light irradiation.

In this work, we propose a multicomponent photocatalyst consisting of reduced graphene oxide wrapped core-shell structured magnetically separable rGO@CuZnO@Fe<sub>3</sub>O<sub>4</sub> microspheres and its successful application for the photoreduction of CO<sub>2</sub> into

methanol under visible light irradiation. The present photocatalyst takes advantage of the high photocatalytic efficiency, high electron mobility, low cost and environmental sustainment of ZnO, the high surface area and superior charge carrier mobility of rGO and the magnetic properties of the core Fe<sub>3</sub>O<sub>4</sub> microspheres to design high efficient and recyclable photocatalyst for the selective reduction of CO<sub>2</sub> into methanol under visible light irradiation.

## 2. Experimental section

### 2.1. Materials

Iron (III) chloride hexahydrate (97%), polyethylene glycol (PEG, Mw~4000), sodium acetate trihydrate (99%), ethylene glycol (99.8%), zinc acetate dihydrate (98%), copper acetate monohydrate (99%), lithium hydroxide (LiOH, 98%), oleic acid (99%), graphite flakes, sodium nitrate (NaNO<sub>3</sub>, 99%), potassium permanganate (KMnO<sub>4</sub>, 99%), dimethylformamide (DMF) and 3-aminopropyltrimethoxysilane (APTMS, 99%) were purchased from Aldrich; they were of analytical grade and used without further purification. Sulfuric acid (H<sub>2</sub>SO<sub>4</sub>), ethanol, hydrochloric acid (HCl, 37%), and hydrogen peroxide (H<sub>2</sub>O<sub>2</sub>) were of analytical grade and purchased from Merck. All other chemicals were of A.R. grade and used without further purification. Graphene oxide (GO) was synthesized by a modified Hummer's method [31].

### 2.2. Techniques used for the chemical and structural characterizations

The rough structure of materials was determined by scanning electron microscopy using FE-SEM (Jeol Model JSM-6340F). The ultrafine structure of materials was determined with High Resolution Transmission Electron Microscopy (HR-TEM) using FEI-TecnaiG<sup>2</sup> Twin TEM operating at an acceleration voltage of 200 kV. It is equipped with a STEM module and an Oxford SDD 80 mm<sup>2</sup> EDX detector. The images were taken with a GATAN Orius 200D for medium resolution and a GATAN UltraScan 1000 for high resolution. The samples for TEM were prepared by depositing a very dilute aqueous suspension of material on carbon coated nickel grid. Fourier transform infrared (FTIR) spectra were recorded on a Perkin–Elmer spectrum RX-1 IR spectrophotometer using potassium bromide window. Raman spectra of materials were collected at room temperature using a Raman Microprobe (HR-800 Jobin–Yvon) with 532 nm Nd-YAG excitation source. The phase structure and crystalline nature of material were determined by powder X-ray diffraction pattern obtained on a Bruker D8 Advance diffractometer at 40 kV and 40 mA with Cu K<sub>α</sub> radiation ( $\lambda=0.15418$  nm). Surface properties of materials like Brunauer–Emmet–Teller surface area (S<sub>BET</sub>), Barret–Joiner–Halenda (BJH) porosity, pore volume etc. were calculated by N<sub>2</sub> adsorption–desorption isotherm at 77 K by using VP-Micromeritics ASAP2010.

XPS measurements were obtained on a KRATOS-AXIS 165 instrument equipped with dual aluminum–magnesium anodes by using MgK<sub>α</sub> radiation ( $h\nu=1253.6$  eV) operated at 5 kV and 15 mA with pass energy of 80 eV and an increment of 0.1 eV. To overcome the charging problem, a charge neutralizer of 2 eV was applied and the binding energy of C<sub>1s</sub> core level (BE  $\approx$  284.6 eV) of adventitious hydrocarbon was used as a standard. The XPS spectra were fitted by using a nonlinear square method with the convolution of Lorentzian and Gaussian functions, after a polynomial background was subtracted from the raw spectra. UV-vis absorption spectra of GO in water (0.03 mg/mL) was collected on Perkin Elmer lambda-19 UV-VIS-NIR spectrophotometer using a 10 mm quartz cell. While for all other solid samples UV-vis spectra were recorded

by making a 1 mm thick pellets using  $\text{BaSO}_4$  as reference. The 333.6 nm line of a 30 mW argon laser was used to record the photoluminescence (PL) spectra at room temperature. The laser beam was focused with a 100 mm focal length lens to produce a 30- $\mu\text{m}$  diameter spot on the sample. The incident power on the sample was 10 mW. The luminescence emitted by the specimen was analyzed by a triple monochromator Dilor RT 30, and then detected using a Hamamatsu R943 photomultiplier in the photon counting mode. Thermal stability and degradation pattern of material were determined by thermogravimetric analysis (TGA) using a thermal analyzer TA-SDT Q-600. Analysis was carried out in the temperature range of 40–800 °C under nitrogen flow with a heating rate of 10 °C/min. Elemental analysis of sample was done on Thermo Scientific™ FLASH 2000 Series CHNS/O Analyzer.

### 2.3. Synthesis of $\text{Fe}_3\text{O}_4$ magnetic microspheres 1

Magnetic  $\text{Fe}_3\text{O}_4$  microspheres were synthesized by following a literature method [32]. Briefly to 40 mL ethylene glycol were added, 1.35 g (5.0 mmol) of iron (III) chloride hexahydrate, 1.0 g PEG<sub>400</sub> and 3.6 g (26.5 mmol) sodium acetate trihydrate and the resulting mixture was stirred to form a clear solution. The obtained solution was transferred in a Teflon lined autoclave and heated at 180 °C for 19 h. After cooling to room temperature, the obtained microspheres were collected by external magnet, washed with water and ethanol, and dried at 60 °C for 8 h.

### 2.4. Synthesis of core-shell $\text{CuZnO@Fe}_3\text{O}_4$ microspheres 2

The core-shell  $\text{CuZnO@Fe}_3\text{O}_4$  microspheres having 1 wt% Cu were synthesized by a modification of literature procedure [33]. In a typical synthesis, 0.1 g of  $\text{Fe}_3\text{O}_4$  microspheres, 0.88 g (4.0 mmol) zinc acetate dihydrate and 0.027 g (0.135 mmol) of copper acetate were added to 80 mL ethanol and sonicated for 10 min. The obtained solution was heated at 70 °C with stirring for 1 h. A separate solution of LiOH was made by dissolving 0.23 g (10.0 mmol) of LiOH in 80 mL of EtOH with stirring for 20 min. Then the ethanolic LiOH solution was added drop-wise to  $\text{Zn}^{2+}$ ,  $\text{Cu}^{2+}$  and  $\text{Fe}_3\text{O}_4$  microspheres containing solution at 0 °C with vigorous stirring. The obtained suspension was sonicated for 5 min and 0.25 mL oleic acid as surfactant was added to prevent agglomeration. The resulting core-shell microspheres were collected by an external magnet and washed thoroughly with water and ethanol followed by drying at 50 °C under vacuum for 5 h for removing the excess of oleic acid from the surface of microspheres. For crystallization of the ZnO shell, the microspheres were subjected to calcination at 500 °C for 8 h. Calcination at higher temperature allowed the removal of residual oleic acid from the surface of microspheres. However, as an effect of higher temperature, the surface –OH group were also removed; thus, for restoration of –OH groups, microspheres were stirred in water for 6 h and dried at 70 °C for 12 h. Furthermore, for the comparison purpose,  $\text{ZnO@Fe}_3\text{O}_4$  microspheres without Cu loading were synthesized and tested for photoreduction of  $\text{CO}_2$  under identical conditions.

### 2.5. Amino-functionalization of $\text{CuZnO@Fe}_3\text{O}_4$ microspheres

The surface of  $\text{CuZnO@Fe}_3\text{O}_4$  microspheres was functionalized with amino functionalities by refluxing 0.1 g  $\text{CuZnO@Fe}_3\text{O}_4$  and 0.1 mL 3-aminopropyl trimethoxysilane (APTMS) in 25 mL ethanol for 24 h. The amino functionalized  $\text{CuZnO@Fe}_3\text{O}_4$  microspheres were separated by an external magnet and washed with ethanol in order to remove unreacted APTMS.

### 2.6. Synthesis of $\text{GO@CuZnO@Fe}_3\text{O}_4$ microspheres 3

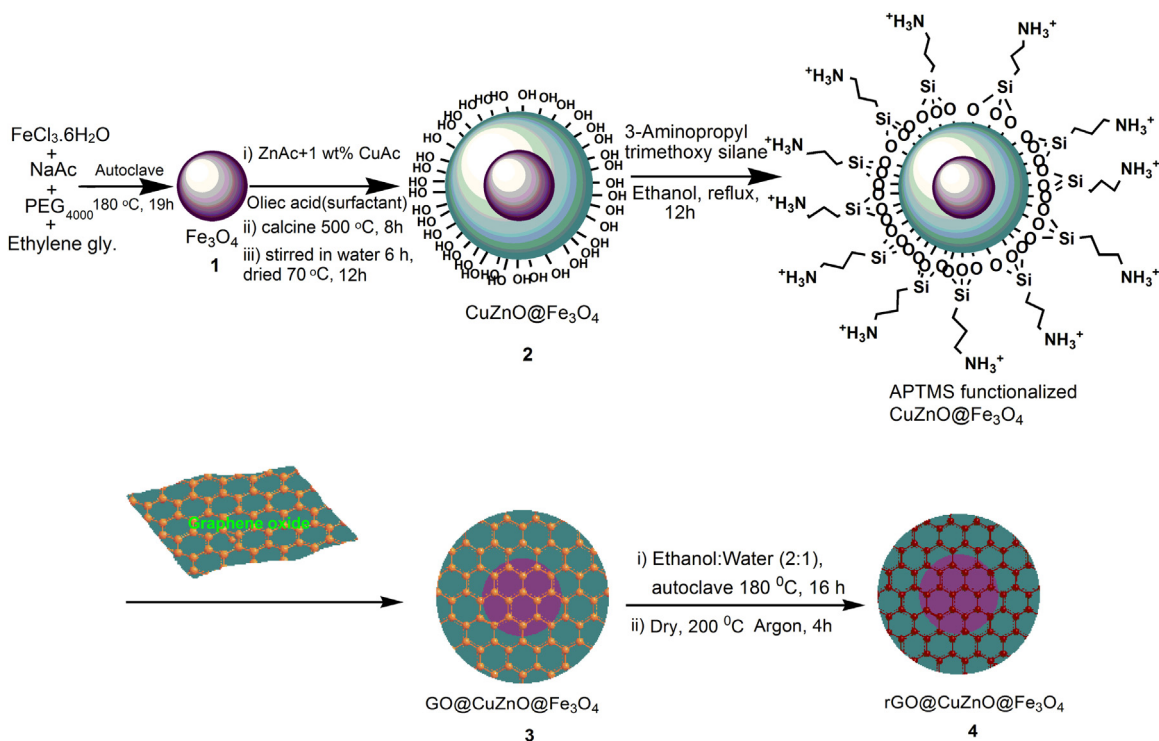
The GO was wrapped on the surface through ionic interaction between positively charged amino functionalized  $\text{CuZnO@Fe}_3\text{O}_4$  2 microspheres and negatively charged GO sheets. In a detail experimental procedure, APTMS functionalized  $\text{CuZnO@Fe}_3\text{O}_4$  microspheres dispersed in 50 mL ethanol were added to 20 mL (0.2 mg/mL) GO aqueous suspension under vigorous stirring at pH 6. After stirring for 30 min, the GO wrapped  $\text{CuZnO@Fe}_3\text{O}_4$  microspheres ( $\text{GO@CuZnO@Fe}_3\text{O}_4$ ) 3 were separated by external magnet, washed with deionized water and dried at 40 °C. Similarly, for a control experiment the corresponding  $\text{GO@ZnO@Fe}_3\text{O}_4$  microspheres without copper were synthesized.

### 2.7. Preparation of $\text{rGO@CuZnO@Fe}_3\text{O}_4$ 4

The  $\text{GO@CuZnO@Fe}_3\text{O}_4$  microspheres 4 were subjected to hydrothermal treatment for effective reduction of GO into reduced graphene oxide. In detail,  $\text{GO@CuZnO@Fe}_3\text{O}_4$  microspheres were dispersed in 30 mL ethanol: water (2:1) solution and transferred in a Teflon-lined stainless steel autoclave. The mixture was heated at 180 °C for 16 h. After cooling to room temperature the suspension was transferred in a beaker and the particles were collected by a magnet, washed with ethanol and dried at 60 °C. Then the particles were calcined at 200 °C for 4 h under argon atmosphere to remove organic impurities. Similarly,  $\text{rGO@CuZnO}$  and  $\text{rGO@ZnO@Fe}_3\text{O}_4$  microspheres were synthesized for comparing the photocatalytic performance.

### 2.8. Photocatalytic reduction of carbon dioxide

The photocatalytic activity of  $\text{rGO@CuZnO@Fe}_3\text{O}_4$  4 and other counterpart components was evaluated using visible light ( $\lambda > 400$  nm) of a 20 W white cold LED light (Model No. HP-FL-20W-F, Hope LED Opto-Electric Co., Ltd. Specification-Chip: KWE, Bridgelux, Epistar COB LED, 20W, Lum output: 80–90 lm/w, Beam angle: 120 degree and wavelength  $\lambda > 400$  nm (maximum at 515 nm). In a 100 mL borosil cylindrical vessel (5 cm dia.), a mixture of DMF and water (45 mL/5 mL) was charged and purged with nitrogen to remove dissolved gases. After that  $\text{CO}_2$  gas was purged in this mixture for 30 min to saturate the solution. Finally, the reaction vessel was charged with 100 mg of catalyst and sealed with a rubber septum. The reaction vessel was placed in a box equipped with magnetic stirrer to prevent from external interference and irradiated with visible light by using LED. The intensity of light on the vessel, measured by intensity meter, was equal to 85  $\text{W m}^{-2}$ . To check the progress of reaction after every 2 h, a sample was withdrawn from the reaction vessel with the help of a needle, and the catalyst was separated by syringe filter (0.2  $\mu\text{m}$  PTFE, 13 mm diameter). The photoreaction products were identified with GC-FID (Varian CP3800 by using CP Sil 24CB LOW BLEED/MS column, flow rate: 0.5  $\text{mL min}^{-1}$ , injector temperature: 250 °C, FID detector temperature: 275 °C). Gaseous products were identified by withdrawing 20  $\mu\text{L}$  sample and analyzed with GC-TCD and GC-FID (Agilent 7890A GC system) using capillary column (RGA, refinery gas analyzer) at the flow rate ( $\text{H}_2$ : 35  $\text{mL min}^{-1}$ , air: 350  $\text{mL min}^{-1}$ , makeup flow: 27  $\text{mL min}^{-1}$ , for TCD reference flow: 45  $\text{mL min}^{-1}$ , Helium flow: 2  $\text{mL min}^{-1}$ ), injector temperature: 220 °C, TCD detector temperature and FID detector temperature: 220 °C. To quantify and check the linear response of GC with different concentrations, a calibration curve was plotted by injecting 1  $\mu\text{L}$  of 50 ppm, 100 ppm, 200 ppm and 500 ppm methanol in GC-FID. Three blank reactions were carried out to confirm that the produced methanol was originated from the  $\text{CO}_2$  photoreduction. For the first blank reaction all conditions were kept identical except without adding photocatalyst to the reaction vessel. In the second blank reaction,



**Scheme 1.** Synthesis of rGO@CuZnO@Fe<sub>3</sub>O<sub>4</sub> microspheres **4**.

photocatalyst and other parameters were same, except the reaction was performed in the dark. While for the third blank reaction, N<sub>2</sub> was purged in place of CO<sub>2</sub>, under otherwise identical conditions. In all three blank reactions no product was formed which confirmed that the produced methanol was the product of CO<sub>2</sub> photoreduction.

### 3. Results and discussion

#### 3.1. Synthesis and characterization of the photocatalyst

The synthetic route of rGO@CuZnO@Fe<sub>3</sub>O<sub>4</sub> microspheres **4** is depicted in **Scheme 1**. At first Fe<sub>3</sub>O<sub>4</sub> microspheres **1** were synthesized by following the already known hydrothermal method using iron(III) chloride hexahydrate as precursor [32]. The core-shell structured CuZnO@Fe<sub>3</sub>O<sub>4</sub> **2** microspheres were prepared by precipitation of zinc acetate and copper acetate solution on Fe<sub>3</sub>O<sub>4</sub> microspheres **1** using lithium hydroxide and oleic acid as surfactant for maintaining spherical geometry of the microspheres, followed by calcination at 500 °C for 8 h [33]. The copper content was maintained to 1 wt% of ZnO. Calcination at higher temperature removed the remaining oleic acid as well as surface –OH groups. The surface –OH groups were restored and maintained in plenty by stirring the sample in water followed by drying at 70 °C. Thus obtained microspheres **2** were subsequently treated with APTMS to get amino functionalized **2**. In the next step, graphene oxide (GO) [31] was wrapped on the surface of –NH<sub>2</sub> functionalized CuZnO@Fe<sub>3</sub>O<sub>4</sub> microspheres through electrostatic interactions [34]. Subsequently GO wrapped microspheres **3** were subjected to hydrothermal treatment at 180 °C for 16 h to get targeted photocatalyst rGO@CuZnO@Fe<sub>3</sub>O<sub>4</sub> **4**. Thus obtained **4** was finally calcined at 200 °C for 4 h under argon atmosphere to remove the residual organic part.

The surface morphology and core-shell structure of microspheres were investigated by FE-SEM imaging (**Fig. 1**). All Fe<sub>3</sub>O<sub>4</sub> particles **1** revealed a spherical morphology with a rough surface;

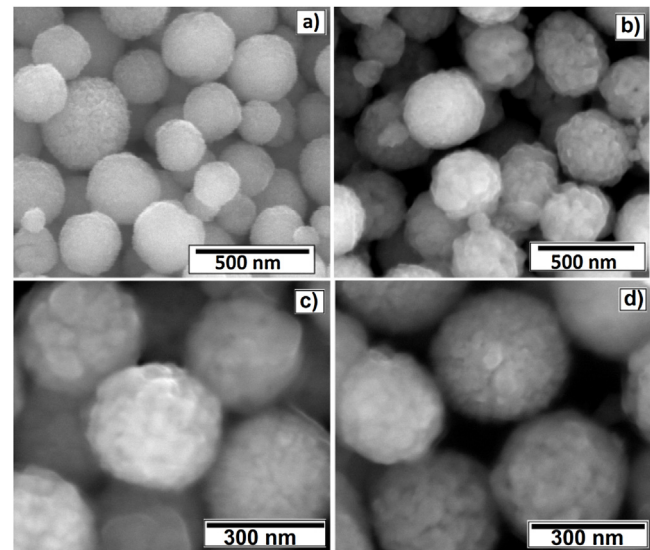


**Fig. 1.** FE-SEM images of a) Fe<sub>3</sub>O<sub>4</sub> **1**, b) CuZnO@Fe<sub>3</sub>O<sub>4</sub> **2**, c) GO@CuZnO@Fe<sub>3</sub>O<sub>4</sub> **3** and d) rGO@CuZnO@Fe<sub>3</sub>O<sub>4</sub> **4**.

their diameter varied between 200 and 250 nm (**Fig. 1a**) [32–34]. After coating with CuZnO the particles remained spherical with some rough outgrowths on the surface and their mean diameter increased up to 300 nm (**Fig. 1b**). Such outgrowths were probably generated during ZnO crystallization upon calcination at 500 °C for 8 h. The SEM image of GO@CuZnO@Fe<sub>3</sub>O<sub>4</sub> **3** revealed similar morphology like CuZnO@Fe<sub>3</sub>O<sub>4</sub> along with wrapped GO sheets on the surface (**Fig. 1c**). The structure of rGO@CuZnO@Fe<sub>3</sub>O<sub>4</sub> **4** remained intact after GO reduction to rGO (**Fig. 1d**).

EDX analysis showed that the samples contained only Fe and O elements for Fe<sub>3</sub>O<sub>4</sub> **1**; Zn, Fe and O elements for CuZnO@Fe<sub>3</sub>O<sub>4</sub> **2**, Cu was not detected may be due to its low concentration in the

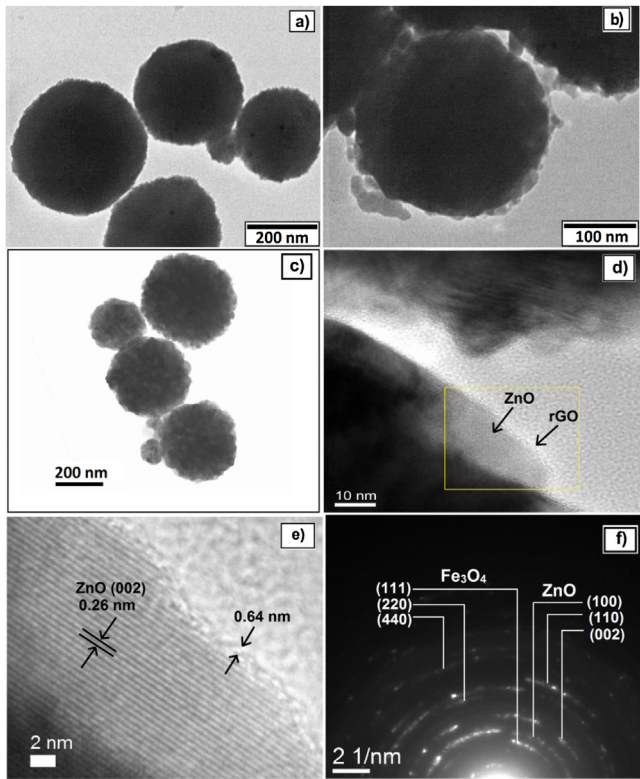


**Fig. 2.** Low resolution TEM images of a)  $\text{Fe}_3\text{O}_4$  **1**, b)  $\text{CuZnO}@\text{Fe}_3\text{O}_4$  **2**, c)  $\text{rGO}@\text{CuZnO}@\text{Fe}_3\text{O}_4$  **4**, d) high magnification TEM of **4**, e) high resolution TEM and f) SAED pattern of  $\text{rGO}@\text{CuZnO}@\text{Fe}_3\text{O}_4$  microspheres **4** showing diffraction patterns of  $\text{Fe}_3\text{O}_4$  and  $\text{ZnO}$ .

material; C, Zn, Fe and O elements for samples **3** and **4** (See Fig. S1, Supplementary Information).

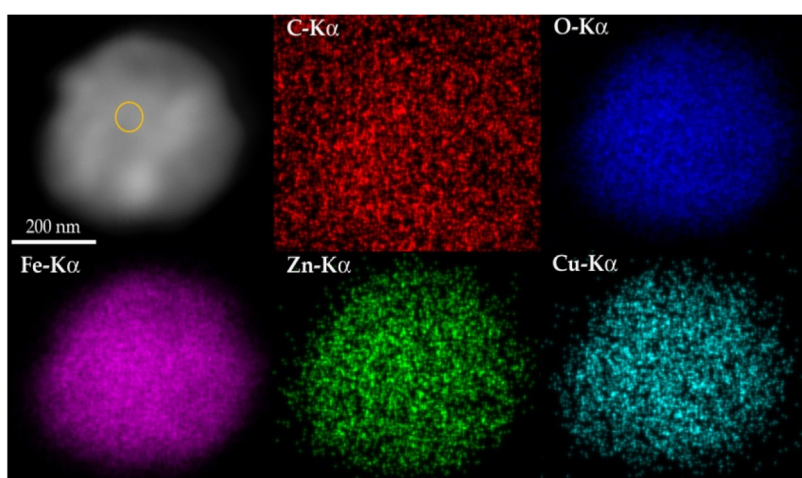
Fine structures of  $\text{Fe}_3\text{O}_4$  **1**,  $\text{CuZnO}@\text{Fe}_3\text{O}_4$  **2** and  $\text{rGO}@\text{CuZnO}@\text{Fe}_3\text{O}_4$  **4** microspheres were examined using TEM imaging (Fig. 2). Low resolution TEM image of **1** exhibited spherical particles of 200–250 nm mean diameter (Fig. 2a). After coating with  $\text{CuZnO}$ , the surface of  $\text{CuZnO}@\text{Fe}_3\text{O}_4$  **2** displayed a rough structure due to  $\text{ZnO}$  deposition, and the particle size slightly increased up to 300 nm (Fig. 2b). High resolution TEM image of  $\text{rGO}@\text{CuZnO}@\text{Fe}_3\text{O}_4$  microspheres **4** showed that particles retained similar rough surface appearance as  $\text{CuZnO}@\text{Fe}_3\text{O}_4$  **2** and their diameter were in the 200–300 nm range (Fig. 2c). The TEM

image of  $\text{rGO}@\text{CuZnO}@\text{Fe}_3\text{O}_4$  **4** at higher magnification clearly evidenced the rough surface and lattice fringes of  $\text{ZnO}$  with the outer amorphous zone attributed to  $\text{rGO}$  (Fig. 2d) [35,36]. The TEM image of the **4** in the high resolution mode clearly exhibited the 1 D lattice plane with 0.26 nm interplanar distance (d-spacing) correlated to (002) plane of  $\text{ZnO}$  (Fig. 2e). In addition, a 0.64 nm of thickness amorphous zone correlated to  $\text{rGO}$  was visible (Fig. 2e). Selected area electron diffraction pattern of microspheres **4** gave diffraction spots corresponding to (111), (220) and (440) planes of  $\text{Fe}_3\text{O}_4$  (JCPDS No. 19–0629) and (100), (110), and (002) planes of  $\text{ZnO}$  (JCPDS No. 36–1451) (Fig. 2f).

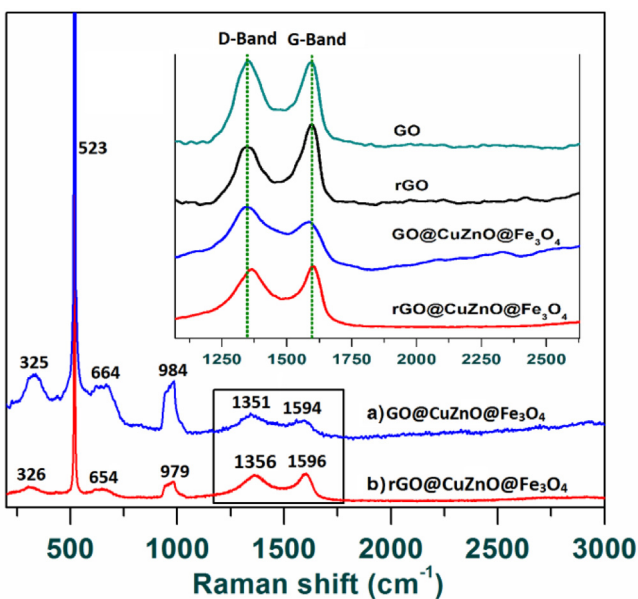
Scanning transmission electron microscopy (STEM) elemental mapping of  $\text{rGO}@\text{CuZnO}@\text{Fe}_3\text{O}_4$  microspheres **4** is depicted in Fig. 3. It could be seen that O, Cu, Zn, Fe and C elements were homogeneously distributed in the material. The presence of an additional carbon zone was most likely due to carbon from the TEM grid. However, a higher concentration of carbon at the microsphere location confirmed the presence of  $\text{rGO}$  sheets. The presence of only C, Cu, Zn, Fe and O in the microspheres was furthermore corroborated by EDX analysis (Fig. S2). A high intensity of carbon was observed as a result of the carbon coated TEM grid.

Fig. 4 exhibits Raman spectra of  $\text{GO}@\text{CuZnO}@\text{Fe}_3\text{O}_4$  **3**,  $\text{rGO}@\text{CuZnO}@\text{Fe}_3\text{O}_4$  microspheres **4** along with GO and rGO spectra. The Raman spectrum of GO revealed specific D ( $1350\text{ cm}^{-1}$ ) and G ( $1593\text{ cm}^{-1}$ ) bands originated from out-plane vibration of  $\text{sp}^3$  carbons presented in the form of defects and in plane vibration of  $\text{sp}^2$  carbons in aromatic conjugated system of GO, respectively. The intensity ratio of D to G bands ( $I_D/I_G$ ) was about 1.01, indicating the presence of many defects in GO in the form of epoxide and other oxygen carrying groups. For rGO the positions of D and G bands were found to be at  $1349$  and  $1593\text{ cm}^{-1}$ , respectively and the integral intensity ratio of D to G bands ( $I_D/I_G$ ) was equal to 0.41. The decrease of D band intensity was attributed to the removal of oxygen carrying functionalities during reduction step and restoration of aromatic conjugated system. For  $\text{GO}@\text{CuZnO}@\text{Fe}_3\text{O}_4$ , the D and G bands of GO were observed at  $1351$  and  $1594\text{ cm}^{-1}$ , respectively with a more intense D band ( $I_D/I_G = 1.13$ ), indicating a large number of defects specific of GO. The decrease of D band ( $1356\text{ cm}^{-1}$ ) intensity in comparison to G band ( $1496\text{ cm}^{-1}$ ) with  $I_D/I_G = 0.87$  after hydrothermal treatment of  $\text{GO}@\text{CuZnO}@\text{Fe}_3\text{O}_4$  **3** confirmed the successful reduction of GO to rGO in **4**.

In addition, the Raman spectrum of  $\text{GO}@\text{CuZnO}@\text{Fe}_3\text{O}_4$  **3** displayed a peak at  $664\text{ cm}^{-1}$  due to  $\text{A}_{1g}$  vibration mode of  $\text{Fe}_3\text{O}_4$  [37] and a band at  $325\text{ cm}^{-1}$  due to  $\text{A}_1$  vibration mode of wurtzite  $\text{ZnO}$  [38]. Some peaks of  $\text{Fe}_3\text{O}_4$  and  $\text{ZnO}$  overlapped. The same peaks



**Fig. 3.** STEM elemental mapping of  $\text{rGO}@\text{CuZnO}@\text{Fe}_3\text{O}_4$  microspheres **4**.



**Fig. 4.** Raman spectra of a) GO@CuZnO@Fe<sub>3</sub>O<sub>4</sub> **3**, b) rGO@CuZnO@Fe<sub>3</sub>O<sub>4</sub> **4**. The insets correspond to the D and G bands of GO and rGO. The sharp peak at 523 cm<sup>-1</sup> is due to silicon substrate.

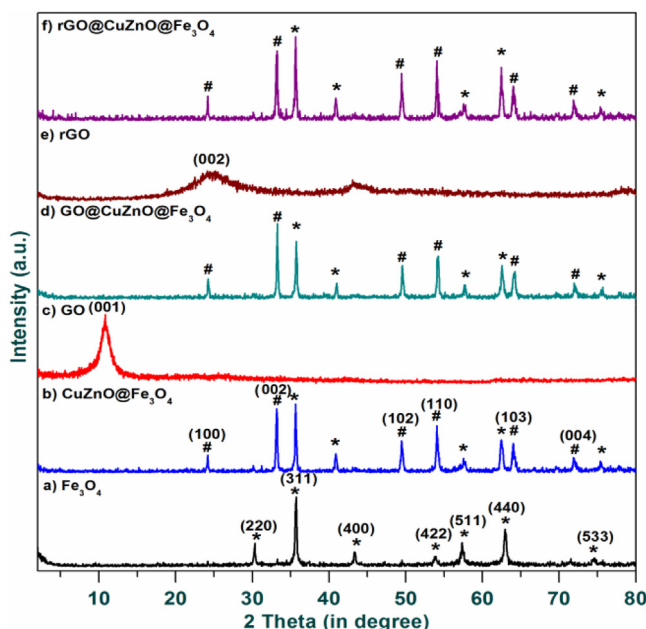


**Fig. 5.** XRD diffraction patterns of a) Fe<sub>3</sub>O<sub>4</sub> **1**, b) CuZnO@Fe<sub>3</sub>O<sub>4</sub> **2**, c) GO, d) GO@CuZnO@Fe<sub>3</sub>O<sub>4</sub> **3**, e) rGO and f) rGO@CuZnO@Fe<sub>3</sub>O<sub>4</sub> **4**.

were observed in the Raman spectrum of rGO@CuZnO@Fe<sub>3</sub>O<sub>4</sub> **4**, indicating the presence of ZnO wurtzite and Fe<sub>3</sub>O<sub>4</sub> magnetite in both samples (Fig. 4).

Powder X-ray diffraction patterns of Fe<sub>3</sub>O<sub>4</sub> **1**, CuZnO@Fe<sub>3</sub>O<sub>4</sub> **2**, GO, GO@CuZnO@Fe<sub>3</sub>O<sub>4</sub> **3**, rGO and rGO@CuZnO@Fe<sub>3</sub>O<sub>4</sub> **4** are depicted in Fig. 5. The XRD pattern of **1** showed characteristic Bragg peaks at 2θ values of 30.32° (220), 35.72° (311), 43.4° (400), 53.92° (422), 57.32° (511), 62.92° (440) and 74.56° (533) matching perfectly with face centered cubic inverse spinel structure of magnetite according to JCPDS No. 19-0629 (Fig. 5a). After coating with 1 wt% copper containing ZnO on Fe<sub>3</sub>O<sub>4</sub> microspheres **1**, the core-shell structured microspheres **2** showed characteristic diffraction peaks of hexagonal wurtzite ZnO along with Fe<sub>3</sub>O<sub>4</sub> diffraction peaks at 2θ:24.20° (100), 33.16° (002), 49.48° (102), 54.04° (110), 64.12°

(103) and 71.84° (004) which was in well conformity with JCPDS No. 36-1451 (Fig. 5b).

No diffraction peak of copper was observed due to its low concentration in comparison to bulk material. Pristine GO gave a sharp peak at 2θ = 11.3° due to diffraction of (001) plane (Fig. 5c). However, no peak of GO was seen in the XRD diffractogram of **3** which indicated the presence of few GO layers in **3** (Fig. 5d). rGO gave a broad hump at 2θ = 24.36° due to (002) carbon plane reflection (Fig. 5e), but this peak was absent in the XRD pattern of rGO@CuZnO@Fe<sub>3</sub>O<sub>4</sub> **4** (Fig. 5f).

X-ray photoelectron spectroscopy (XPS) was used to follow the changes in the chemical composition at each stage of material modification (Fig. 6). Survey scans of microspheres **3** and **4** exhibited peaks at 285, 530, 400, 710, 1022 and 103 eV due to C<sub>1s</sub>, O<sub>1s</sub>, N<sub>1s</sub>, Fe<sub>2p</sub>, Zn<sub>2p</sub> and Si<sub>2p</sub>, respectively. The peak of copper due to its lower concentration may not be appearing in the XPS; however, its presence was confirmed by EDX (Fig. 3). The atomic percentages of different components are given in Table S1; the carbon atomic percentage was estimated to be 56.16% and 48.50% for microsphere **3** and **4**, respectively. Higher value of carbon concentration suggested the presence of carbon sheets on the surface of **4**. Furthermore, the presence of small amount of Si<sub>2p</sub> and N<sub>1s</sub> was detected due to the APTMS linker. C<sub>1s</sub> high resolution XPS spectrum of microspheres **3** exhibited characteristic peak components of GO at 285.1, 286.6 and 289.0 eV due to C–C, C–O and –COOH groups, respectively with an additional peak at 283.7 eV due C–Si group (Fig. 6a). After hydrothermal reduction, the C<sub>1s</sub> wide scan of microspheres **4** showed a decrease of –COOH peak intensity at 289.0 eV, suggesting the successful reduction of GO to rGO (Fig. 6b).

Fe<sub>2p</sub> high resolution XPS spectrum of microspheres **4** displayed two characteristic peaks due to Fe<sub>2p3/2</sub> and Fe<sub>2p1/2</sub> at 711.5 and 724.8 eV, respectively, in concordance with literature values for Fe<sub>3</sub>O<sub>4</sub> (Fig. 6c). Further, a satellite peak was observed at 718 eV attributed due to presence very thin oxide's layer of Fe<sub>2</sub>O<sub>3</sub> on the surface of microspheres. In addition, the peaks at 1022.0 and 1043.1 eV due to Zn<sub>2p3/2</sub> and Zn<sub>2p1/2</sub>, respectively confirmed the presence of ZnO on the surface of microspheres **4** (Fig. 6d). We did not observe any peak due to Cu, because of its low concentration in comparison to ZnO in the composite.

UV-vis absorption spectra of solid samples are shown in (Fig. 7a). UV-vis absorption spectrum of magnetic Fe<sub>3</sub>O<sub>4</sub> core and Fe<sub>2</sub>O<sub>3</sub> present on surface of microspheres. Nanoparticles gave a broad absorption profile from 200 to 650 nm, due to d-orbital transitions of Fe<sub>3</sub>O<sub>4</sub> [39–41]. ZnO synthesized for comparison by similar method gave a sharp absorption band at 370 nm and thus absorbs only in UV region. The core-shell CuZnO@Fe<sub>3</sub>O<sub>4</sub> microspheres **2** displayed a broad absorption band from 200 to 560 nm similar to pure Fe<sub>3</sub>O<sub>4</sub> but the intensity started to decrease after 560 nm due to the coating of ZnO. After wrapping of GO sheets on CuZnO@Fe<sub>3</sub>O<sub>4</sub> microsphere **2**, the visible light absorption pattern slightly decreased in GO@CuZnO@Fe<sub>3</sub>O<sub>4</sub> **3** as GO sheets could not absorb in visible region. Further for rGO wrapped rGO@CuZnO@Fe<sub>3</sub>O<sub>4</sub> microspheres **4** the absorption pattern increased in visible region due to the synergistic effect.

The optical band gap of the Fe<sub>3</sub>O<sub>4</sub> **1**, ZnO, CuZnO@Fe<sub>3</sub>O<sub>4</sub> **2**, GO@CuZnO@Fe<sub>3</sub>O<sub>4</sub> **3** and rGO@CuZnO@Fe<sub>3</sub>O<sub>4</sub> **4** was calculated by extrapolating the rising segment of the UV spectrum to the abscissa at zero absorption with the help of the Tauc plot (Fig. 7b). Although Fe<sub>3</sub>O<sub>4</sub> is semi-metal and doesn't possess a band gap at 300 K but during synthesis and oxidation in air a very thin layer of oxide (Fe<sub>2</sub>O<sub>3</sub>) was obtained on the surface of Fe<sub>3</sub>O<sub>4</sub> microspheres. So, due to presence of Fe<sub>2</sub>O<sub>3</sub> on the surface of Fe<sub>3</sub>O<sub>4</sub> microspheres can work as semiconductor [42]. In our case a band gap value of **1** was found to be 1.16 eV which was low enough for visible light mediated transition. The value of the band gap of pure sample of ZnO was 3.20 eV (corresponding to 386 nm), which indicates that

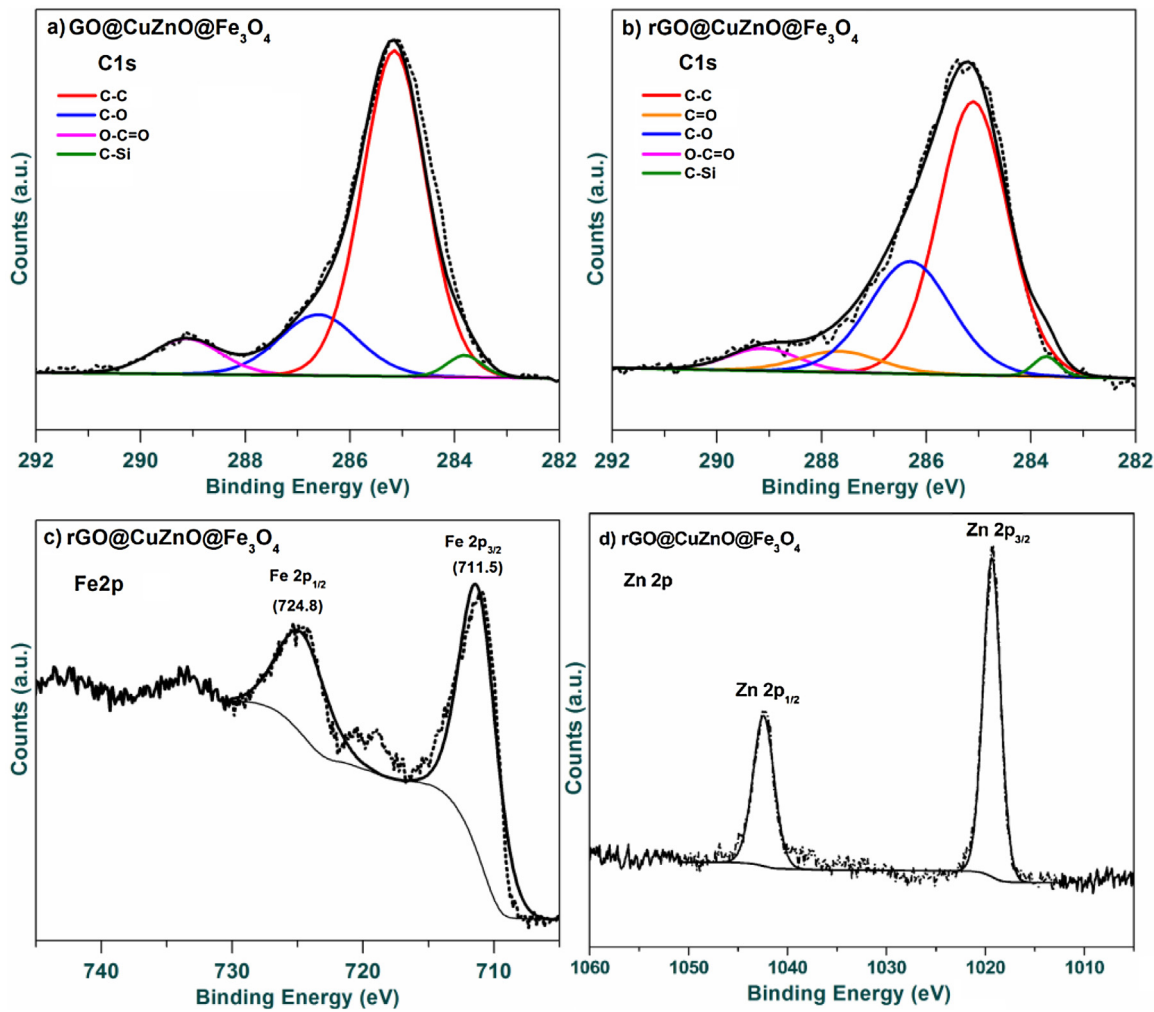


Fig. 6. C<sub>1s</sub> high resolution XPS spectra of a) GO@CuZnO@Fe<sub>3</sub>O<sub>4</sub> **3**, b) rGO@CuZnO@Fe<sub>3</sub>O<sub>4</sub> **4**, c) Fe<sub>2p</sub> and d) Zn<sub>2p</sub> of rGO@CuZnO@Fe<sub>3</sub>O<sub>4</sub> **4**.

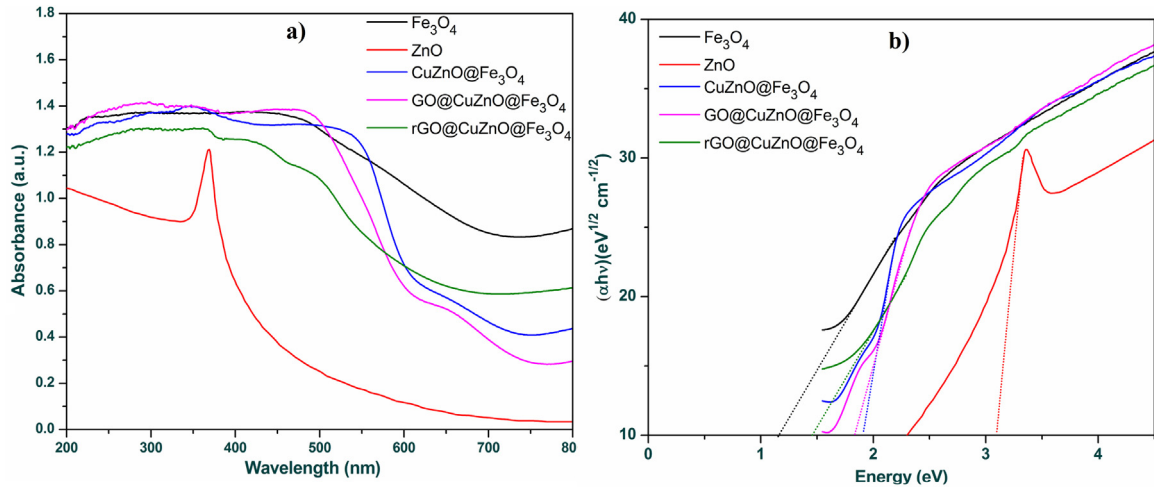
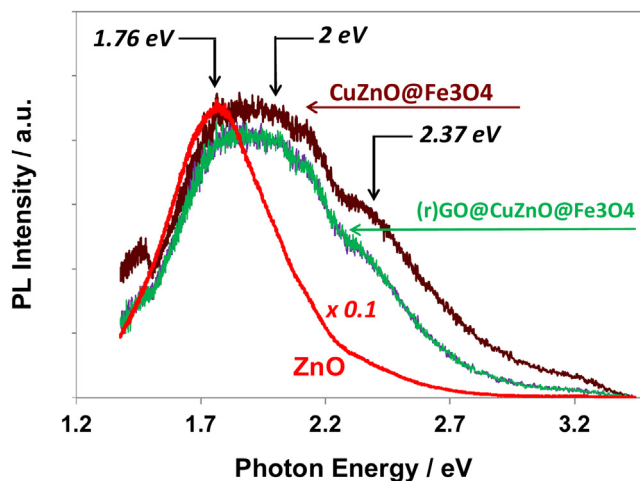


Fig. 7. UV-vis absorption spectra a) and Tauc plot showing band gap b) of Fe<sub>2</sub>O<sub>3</sub>/Fe<sub>3</sub>O<sub>4</sub> **1**, CuZnO@Fe<sub>3</sub>O<sub>4</sub> **2**, GO@CuZnO@Fe<sub>3</sub>O<sub>4</sub> **3**, rGO@CuZnO@Fe<sub>3</sub>O<sub>4</sub> **4**.

it can absorb only in the UV region. The obtained band gap value was found to be slightly lower than the reported value (3.3 eV) which is most likely due to the presence of some defects [43]. After the coating of ZnO on the Fe<sub>3</sub>O<sub>4</sub> microspheres the value of the band gap increased to 1.9 eV associated with 651 nm wavelength. The GO wrapped particles GO@CuZnO@Fe<sub>3</sub>O<sub>4</sub> **3** displayed a band

gap of 1.85 eV (corresponding wavelength: 669 nm). Hydrothermal treatment of **3** transformed wrapped GO to rGO and the band gap value decreased to 1.44 eV for rGO@CuZnO@Fe<sub>3</sub>O<sub>4</sub> **4** which was correlated to 859 nm wavelength. The reduced band gap value for microspheres **4** confirmed their visible light absorption potential.



**Fig. 8.** Photoluminescence spectra of ZnO (red), CuZnO@Fe<sub>3</sub>O<sub>4</sub> (dark red) **2**, GO@CuZnO@Fe<sub>3</sub>O<sub>4</sub> **3** (green) and rGO@CuZnO@Fe<sub>3</sub>O<sub>4</sub> **4** (blue). (For interpretation of the references to colour in this figure legend, the reader is referred to the web version of this article.)

The PL spectra of the different samples are depicted in Fig. 8. Three important observations can be made: (i) the integral luminescence intensity (IPL<sub>tot</sub>) of ZnO is about 6 times that of the other three samples (CuZnO@Fe<sub>3</sub>O<sub>4</sub>, GO@CuZnO@Fe<sub>3</sub>O<sub>4</sub> and rGO@CuZnO@Fe<sub>3</sub>O<sub>4</sub>), (ii) IPL<sub>tot</sub> of CuZnO@Fe<sub>3</sub>O<sub>4</sub> is about 1.3 times that of GO@CuZnO@Fe<sub>3</sub>O<sub>4</sub> and of rGO@CuZnO@Fe<sub>3</sub>O<sub>4</sub> which are identical, (iii) the spectral shape of ZnO is very different from the three other ones which are nearly identical. Its full width at half maximum (FWHM) is close to 0.5 eV, whereas it is as large as 0.8 eV in both GO@CuZnO@Fe<sub>3</sub>O<sub>4</sub> **3** and rGO@CuZnO@Fe<sub>3</sub>O<sub>4</sub> **4** and equal to 1 eV in CuZnO@Fe<sub>3</sub>O<sub>4</sub>. Furthermore, its shape is very asymmetric, with a main red PL band at 1.76 eV (704 nm). On the opposite, the shape of the other three PL spectra is more symmetrical. In fact, additionally to the red band at 1.8 eV, there is a red/orange band of similar intensity which is close to 2 eV (620 nm). Furthermore, a green band close to 2.4 eV is also visible. The spectra extend until about 3.4 eV. The green band close to 2.4 eV which appears as a hump in the PL spectra is certainly due to copper [44–46]. The origin of the red emission is more controversial since it was associated with zinc interstitials [47], zinc vacancies [48] or excess oxygen [49]. The red/orange emission is usually attributed to oxygen interstitial defects [50] or to excess oxygen [51].

### 3.2. Photocatalytic activity

The photocatalytic performance of rGO@CuZnO@Fe<sub>3</sub>O<sub>4</sub> microspheres **4** and other components such as GO, rGO, ZnO, CuZnO, Fe<sub>3</sub>O<sub>4</sub> **1**, ZnO@Fe<sub>3</sub>O<sub>4</sub>, CuZnO@Fe<sub>3</sub>O<sub>4</sub> microspheres **2** and GO@ZnO@Fe<sub>3</sub>O<sub>4</sub> **3** for CO<sub>2</sub> photoreduction was evaluated in DMF/water (45/5 mL) using a 20 W white cold LED as visible light source (see more details in experimental section). The results of these experiments are summarized in Table 1. For the identification and quantification of products, 1  $\mu$ L liquid sample was withdrawn at every 2 h interval and analyzed by GC-FID. The GC analysis showed that methanol was formed as the major liquid reaction product without any evidence for the formation of other possible reaction products like formic acid, ethanol, etc (Fig. S6). A calibration curve was plotted by injecting calculated amount of methanol in GC for quantification and checking linear response of GC toward various concentrations of methanol (Fig. S7). Gaseous products were analyzed by injecting 20  $\mu$ L of sample in GC-TCD and GC-FID by using RGA column. Gaseous product analysis showed that hydrogen was evolved in very small amount; other products if

any like methane, CO, etc were not detected under our experimental conditions. As methanol was the only liquid reaction product, a graph between methanol yield ( $\mu$ mol g<sup>-1</sup> cat) and reaction time was plotted to determine the catalyst performance as compared to other catalyst components (Figs. 10 and 11). After 24 h visible light irradiation of a CO<sub>2</sub> saturated DMF/water solution, the yield of methanol by using Fe<sub>3</sub>O<sub>4</sub> microspheres **1**, CuZnO@Fe<sub>3</sub>O<sub>4</sub> **2**, GO@CuZnO@Fe<sub>3</sub>O<sub>4</sub> **3** and rGO@CuZnO@Fe<sub>3</sub>O<sub>4</sub> **4** was determined to be 278, 858, 1749 and 2656  $\mu$ mol g<sup>-1</sup> cat, respectively. The methanol formation rate ( $R_{\text{MeOH}}$ ) for **1**, **2**, **3** and **4** was found to be 11.6, 35.7, 72.9 and 110.6  $\mu$ mol h<sup>-1</sup> g<sup>-1</sup> cat, respectively. The associated quantum yield ( $\phi_{\text{MeOH}}$ ) for methanol was estimated to be 0.0026, 0.0082, 0.0167 and 0.0253 mole einstein<sup>-1</sup>, respectively.

The quantum yield of product was determined by using following formula:

$$\phi_{\text{product}} = [P] \times n / [\gamma]$$

Where,  $\phi_{\text{product}}$  is quantum yield, [P] is moles of desired product, n is number of electrons required for reduction and  $[\gamma]$  is moles of incident photons.

For methanol and hydrogen formation, the number of electrons required is 6 and 2, respectively.

The analysis of gaseous products provided the hydrogen yield as 16.2, 28.5 and 45.5  $\mu$ mol g<sup>-1</sup> cat for CuZnO@Fe<sub>3</sub>O<sub>4</sub> **2**, GO@CuZnO@Fe<sub>3</sub>O<sub>4</sub> **3** and rGO@CuZnO@Fe<sub>3</sub>O<sub>4</sub> **4**, respectively with formation rate ( $R_{\text{H}_2}$ ) of 0.6, 1.2 and 1.9  $\mu$ mol h<sup>-1</sup> g<sup>-1</sup> cat, respectively.

The catalytic selectivity was determined by:

$$\text{CS\%} = [P] \times 100 / [P_{\text{total}}]$$

Where CS% is the catalytic selectivity in%, [P] is moles of desired product; [P<sub>total</sub>] is moles of total reaction products.

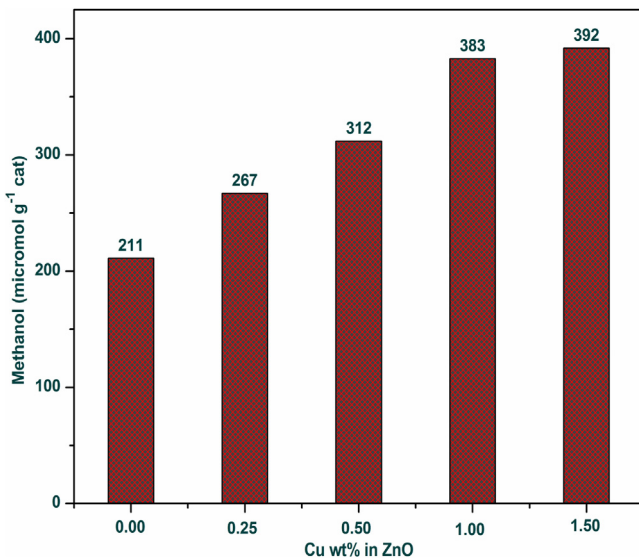
The catalytic selectivity in percentage (CS%) of Fe<sub>3</sub>O<sub>4</sub> microspheres **1**, CuZnO@Fe<sub>3</sub>O<sub>4</sub> microspheres **2**, GO@CuZnO@Fe<sub>3</sub>O<sub>4</sub> microspheres **3** and rGO@CuZnO@Fe<sub>3</sub>O<sub>4</sub> microspheres **4** for methanol was determined to be 100, 94.14, 98.39 and 98.31, respectively.

The efficiency of the developed rGO@CuZnO@Fe<sub>3</sub>O<sub>4</sub> photocatalyst **4** for CO<sub>2</sub> photoreduction was much higher than those reported in the literature for different photocatalysts. A comparison of the photocatalytic performance of **4** with the state of the art photocatalysts for CO<sub>2</sub> reduction is presented in Table S2.

As can be seen in Table 1 only a very small amount of methanol can be detected for rGO due to the absence of band gap (zero band gap) [52] so it was unable to generate electron and hole pairs which are essential for photoreduction of CO<sub>2</sub>. However, the origin of small amount of methanol (117  $\mu$ mol g<sup>-1</sup> cat) can be explained on the basis of residual oxygen functionalities which remained after the reduction of GO to rGO. Owing to the presence of sp<sup>2</sup> and sp<sup>3</sup> carbons on its surface, rGO acted like a semiconductor. The sp<sup>2</sup> hybridized carbon containing domains due to the free mobility of electrons behave like a conduction band while sp<sup>3</sup> carbon containing domains due to tightly held electrons behave like a valence band. But the number of such sp<sup>2</sup> and sp<sup>3</sup> domains in rGO is less in comparison to GO therefore poor yield of methanol was obtained. The band gap value of GO was found to be in the range of 2.8–3.6 eV due to the uneven oxidation which is in well concordance with literature values [53]. ZnO has larger band gap (3.3 eV) which is high enough to prevent any visible light mediated transition [43]. However, a small amount of methanol (211  $\mu$ mol g<sup>-1</sup> cat) may be originated due to the presence of some defects in ZnO. Addition of copper enhances the photocatalytic performance of ZnO by capturing electrons from the conduction band of ZnO which delayed the charge recombination process, so the electron availability for the reduction of CO<sub>2</sub> was increased [54,55]. To evaluate the optimal

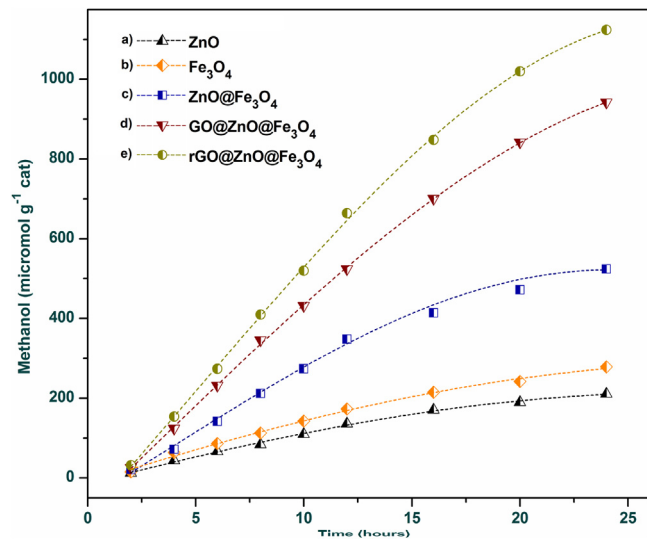
**Table 1**Photocatalytic reduction of  $\text{CO}_2$  by using different catalysts.<sup>a</sup>

Entry	Catalyst	Reactant	Methanol Yield ( $\mu\text{mol g}^{-1}\text{cat}$ )	Quantum Yield (mole einstien $^{-1}$ )
1	Blank	$\text{CO}_2$	Nil <sup>b</sup>	Nil
2	$\text{Fe}_3\text{O}_4$ <b>1</b>	$\text{CO}_2$	278	0.0026
3	$\text{ZnO}$	$\text{CO}_2$	211	0.0020
4	1 wt% $\text{CuZnO}$	$\text{CO}_2$	383	0.0036
5	GO	$\text{CO}_2$	470	0.0044
6	rGO	$\text{CO}_2$	117	0.0011
7	rGO@CuZnO	$\text{CO}_2$	648	0.0061
8	$\text{ZnO}@\text{Fe}_3\text{O}_4$	$\text{CO}_2$	524	0.0049
9	$\text{CuZnO}@\text{Fe}_3\text{O}_4$ <b>2</b>	$\text{CO}_2$	858	0.0082
10	$\text{GO}@\text{ZnO}@\text{Fe}_3\text{O}_4$	$\text{CO}_2$	942	0.0089
11	$\text{rGO}@\text{ZnO}@\text{Fe}_3\text{O}_4$	$\text{CO}_2$	1124	0.0106
12	$\text{GO}@\text{CuZnO}@\text{Fe}_3\text{O}_4$ <b>3</b>	$\text{CO}_2$	1749	0.0167
13	$\text{rGO}@\text{CuZnO}@\text{Fe}_3\text{O}_4$ <b>4</b>	$\text{CO}_2$	2656	0.0253
		$\text{N}_2$	Nil	Nil
		$\text{CO}_2$	Nil	Nil

<sup>a</sup> Reaction conditions: catalyst: 100 mg, solvent: DMF/water (45/5), visible light irradiation using 20 W LED ( $\lambda > 400$  nm), time: 24 h.<sup>b</sup> Without catalyst.**Fig. 9.** Methanol yield using 0.25, 0.50, 1.00 and 1.50 wt% of copper loaded  $\text{ZnO}$  ( $\text{CuZnO}$ ).

loading of Cu we synthesized a number of  $\text{CuZnO}$  composites having 0.25, 0.5, 1.0 and 1.5 wt% of copper. It can be seen from Fig. 9 that the yield of methanol increased with increasing the copper loading from 0.25 to 1.0 wt%, however further increase of Cu content did not influence the photocatalytic performance. The yield of methanol by using 0.25, 0.50, 1.0 and 1.5 wt% of copper loaded  $\text{ZnO}$  ( $\text{CuZnO}$ ) was found to be 267, 312, 383 and 392  $\mu\text{mol g}^{-1}\text{cat}$ , respectively. The enhancement in the methanol yield with copper content was assumed to be due to the trapping of photogenerated electrons which resulted in reduced electron-hole pair recombination. Based on these results we have chosen 1.0 wt%  $\text{CuZnO}$  as the optimal for coating on  $\text{Fe}_3\text{O}_4$  microspheres **1**.

In case of  $\text{Fe}_3\text{O}_4$  microspheres **1**, a very poor yield of methanol 278  $\mu\text{mol g}^{-1}\text{cat}$  was obtained due to presence of  $\text{Fe}_2\text{O}_3$  layer on microspheres (Fig. 10b). In order to check the synergistic effect of the components in the designed composite **4** on  $\text{CO}_2$  photoreduction, we synthesized all the possible combinations such as  $\text{ZnO}@\text{Fe}_3\text{O}_4$ ,  $\text{GO}@\text{ZnO}@\text{Fe}_3\text{O}_4$  and  $\text{rGO}@\text{ZnO}@\text{Fe}_3\text{O}_4$  and evaluated their performance for the photoreduction of  $\text{CO}_2$  under described experimental conditions. The yield of methanol by using  $\text{ZnO}@\text{Fe}_3\text{O}_4$ ,  $\text{GO}@\text{ZnO}@\text{Fe}_3\text{O}_4$  and  $\text{rGO}@\text{ZnO}@\text{Fe}_3\text{O}_4$  microspheres as photocatalysts was found to be 524, 942 and 1124  $\mu\text{mol g}^{-1}\text{cat}$ , respectively after 24 h of visible irradiation. For  $\text{ZnO}@\text{Fe}_3\text{O}_4$  micro-

**Fig. 10.**  $\text{CO}_2$  conversion to methanol for a)  $\text{ZnO}$ , b)  $\text{Fe}_3\text{O}_4$  **1** c)  $\text{ZnO}@\text{Fe}_3\text{O}_4$  microspheres, d)  $\text{GO}@\text{ZnO}@\text{Fe}_3\text{O}_4$  microspheres, and e)  $\text{rGO}@\text{ZnO}@\text{Fe}_3\text{O}_4$  microspheres.

spheres the enhancement of yield can be explained by the efficient transfer of photogenerated electrons and holes of  $\text{Fe}_2\text{O}_3/\text{Fe}_3\text{O}_4$  to the conduction and valence band of  $\text{ZnO}$ , respectively (Fig. 10c). Further, the wrapping of GO on  $\text{ZnO}@\text{Fe}_3\text{O}_4$  microspheres enhances the yield of methanol which is believed to be due to the transfer of electrons from CB of  $\text{ZnO}$  to GO sheets (Fig. 10d). Reduction of wrapped GO to rGO further enhances the yield of methanol because of the restoration of  $\text{sp}^2$  hybridized aromatic system in rGO which provides better electron mobility as well as charge separation in comparison to GO where the presence of  $\text{sp}^3$  carbons restricts the free movement of the electrons on the GO sheets (Fig. 10e). Furthermore, the yield of methanol by using  $\text{rGO}@\text{CuZnO}$  as photocatalyst was found to be 648  $\mu\text{mol g}^{-1}\text{cat}$  which confirms that the coating of rGO played an important role in facilitating the charge separation.

As shown in the previous section that the presence of copper enhanced the photocatalytic performance and methanol yield. To establish the promoting effect of copper, we compared the photocatalytic activity of **2** and **3** with **4** (Fig. 11). No methanol was formed in the blank reaction in the absence of photocatalyst (Fig. 11a). However, the methanol yield using 1 wt%  $\text{CuZnO}$  was found to be 383  $\mu\text{mol g}^{-1}\text{cat}$  (Fig. 11b). The methanol yield for  $\text{CuZnO}@\text{Fe}_3\text{O}_4$  microspheres **2** was determined to be 858  $\mu\text{mol g}^{-1}\text{cat}$  (Fig. 11c). The increase in yield was attributed to the transfer of electrons and holes from  $\text{Fe}_2\text{O}_3/\text{Fe}_3\text{O}_4$  to the CB and VB of  $\text{ZnO}$  followed

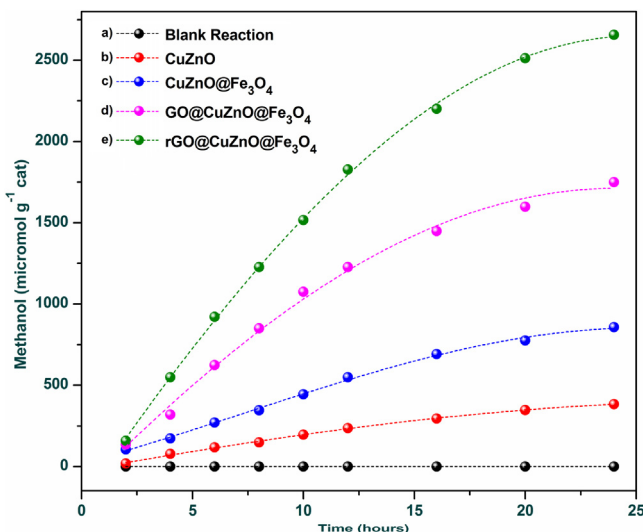


**Fig. 11.** Yield of methanol, a) blank reaction, b) using 1 wt% CuZnO, c) CuZnO@Fe<sub>3</sub>O<sub>4</sub>, 2, d) GO@CuZnO@Fe<sub>3</sub>O<sub>4</sub> **3**, and e) rGO@CuZnO@Fe<sub>3</sub>O<sub>4</sub> **4**.

by electron capturing by Cu, which prevents charge recombination. Because, CuZnO was coated on Fe<sub>3</sub>O<sub>4</sub> microspheres by *in situ* method, we assume that copper was evenly distributed in the ZnO layer of the composite. XPS analysis of the nanocomposite did not show any peak of the Cu due to its low concentration in comparison to ZnO, which confirms that Cu is not limited to ZnO surface but it is also present in the bulk volume of ZnO (Fig. 6 and Table S1). Moreover, STEM elemental mapping and EDX analysis of microspheres **4** clearly showed the presence of Cu because of the deeper penetration by electron beam, so more Cu atoms are encountered in path, confirming that Cu was homogeneously distributed in the ZnO layer (Figs. 3 and S2). Despite that the Cu embedded in ZnO also takes part in electron capturing process, it does not participate in electron transfer to the GO/rGO due to deactivation of charge by the process of volume recombination. Only the Cu present on the ZnO surface can transfer captured electrons to rGO. The GO wrapped GO@CuZnO@Fe<sub>3</sub>O<sub>4</sub> microspheres **3** afforded 1749  $\mu\text{mol g}^{-1}$  cat of methanol which was much higher than **2** due to the transfer of electrons to GO surface (Fig. 11d). The highest yield of methanol was obtained for rGO@CuZnO@Fe<sub>3</sub>O<sub>4</sub> microspheres **4** up to 2656  $\mu\text{mol g}^{-1}$  cat because of better mobility of electrons on reduced graphene oxide surface which maintains the sufficient distance between the electrons and thus slows down charge recombination process (Fig. 11e).

The synthesized rGO@CuZnO@Fe<sub>3</sub>O<sub>4</sub> (**4**) could be easily recovered by using external magnet for recycling experiments. Fig. 12a and b showed that the catalyst was well dispersed in absence of any magnetic field, while after exposure to 1 T magnet for 1 min the coloured solution became nearly transparent.

Furthermore, we performed recycling experiments in order to check the reusability of the rGO@CuZnO@Fe<sub>3</sub>O<sub>4</sub> **4** photocatalyst. After completion of the reaction, the photocatalyst was separated by using a magnet, washed with water and reused for subsequent CO<sub>2</sub> photoreduction experiment. It can be seen from Fig. 12 that there was no significant loss in activity even after five recycling experiments. However, a slight decrease in the photocatalytic performance after few recycling runs was attributed to removal of some rGO sheets from the surface of **4** under vigorous stirring condition. To confirm the loss of rGO sheets from **4**, we performed elemental analysis of freshly synthesized and recovered photocatalyst after fifth run to determine the carbon content. The carbon content of freshly synthesized **4** was 3.67 wt% while after five recycling the carbon content was 3.43 wt%. This small decrease

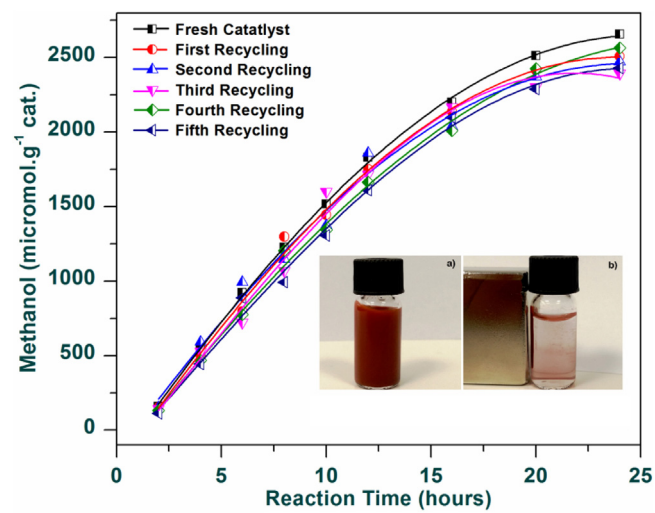
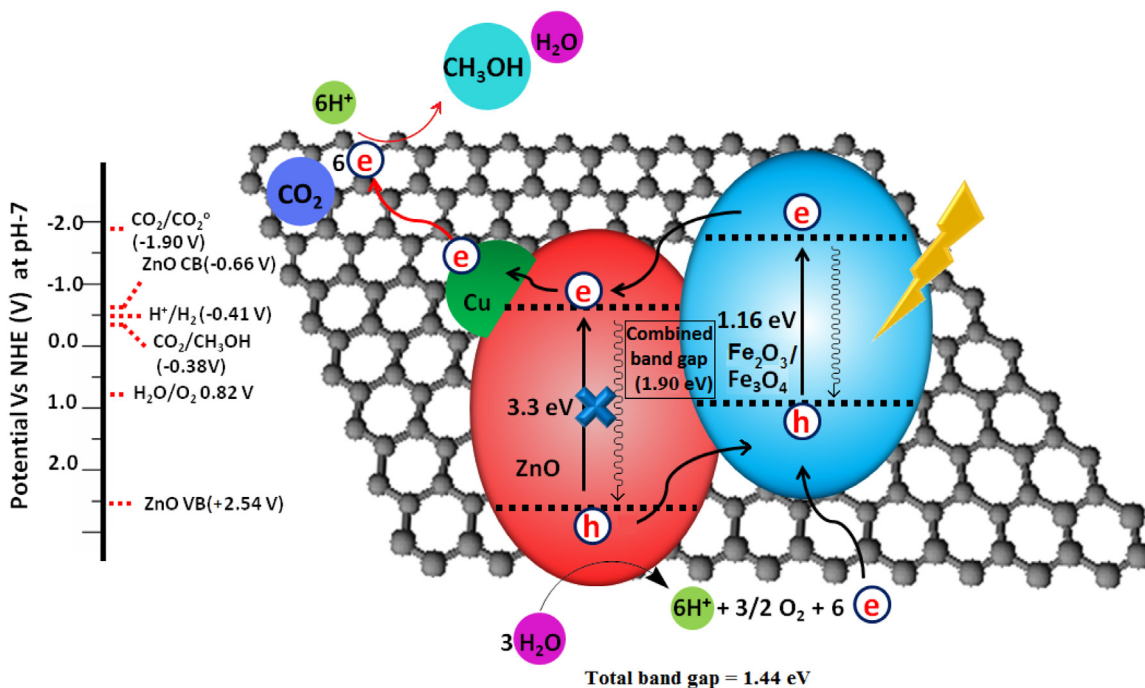


**Fig. 12.** Recycling experiments using rGO@CuZnO@Fe<sub>3</sub>O<sub>4</sub> microspheres **4**. Inset showing magnetic separation experiments: a) rGO@CuZnO@Fe<sub>3</sub>O<sub>4</sub> microspheres **4** dispersed in water and b) after exposure to 1 T magnet for 1 min.

(0.24 wt%) in C% revealed that some sheets of rGO were removed from the surface of **4** during the stirring condition of reaction and resulted in the decrease of efficiency.

On the basis of band gap, a plausible mechanism was proposed for enhanced activity of rGO@CuZnO@Fe<sub>3</sub>O<sub>4</sub> microspheres **4** for CO<sub>2</sub> reduction (Scheme 2). For the CO<sub>2</sub> reduction to methanol the position of conduction band of semiconductor should be more negative than reduction potential of CO<sub>2</sub>/CH<sub>3</sub>OH (−0.38 V vs NHE at pH 7) and the position of valence band should be more positive than oxidation potential of H<sub>2</sub>O/O<sub>2</sub> (+0.82 V vs NHE at pH 7) [3]. This means that the band gap of the semiconductor should be wide so both CO<sub>2</sub> reduction and water oxidation reaction can proceed simultaneously. Fe<sub>3</sub>O<sub>4</sub> microspheres due to presence of Fe<sub>2</sub>O<sub>3</sub> layer on the surface works as semiconductor and can produce electron hole pairs in visible light [42], but due to the narrow band gap (1.16 eV) they are unable to achieve water splitting. ZnO has a wide band gap (3.2 eV) with suitable positions of conduction band (−0.66 V vs NHE at pH 7) and valence band (+2.54 V vs NHE at pH 7) to reduce CO<sub>2</sub> to methanol and oxidize water to oxygen, respectively [55]. However, only UV light can make transition of electrons from valence to conduction band. So neither Fe<sub>3</sub>O<sub>4</sub> nor ZnO alone could reduce CO<sub>2</sub> to methanol. However, when ZnO was coated on Fe<sub>3</sub>O<sub>4</sub> the obtained microspheres can reduce CO<sub>2</sub> to methanol and achieve water splitting which can be explained on the basis of reduced band gap (1.90 eV) for CuZnO@Fe<sub>3</sub>O<sub>4</sub> microspheres and synergistic mechanism of electron-hole pairs generation. After absorption of visible light, Fe<sub>2</sub>O<sub>3</sub> present on the surface of Fe<sub>3</sub>O<sub>4</sub> get excited and electron-hole pairs were produced in the conduction and valence band, respectively. Electrons from the conduction band of Fe<sub>2</sub>O<sub>3</sub>/Fe<sub>3</sub>O<sub>4</sub> move to the conduction band of ZnO while holes move to valence band of ZnO so indirectly electrons and holes were produced in CB and VB of ZnO, respectively. But due to electron-hole pair recombination the yield of methanol was found to be poor. *In-situ* addition of Cu slowed down the process of electron-hole pair recombination by capturing photogenerated electrons by the Cu present on the surface of the microspheres. GO wrapping further increases the photocatalytic performance of CuZnO@Fe<sub>3</sub>O<sub>4</sub> because of efficient capturing of electrons by GO. After reduction GO to rGO on microspheres the combined band gap of matrix was found to be 1.44 eV. Wrapping of rGO not only reduces the band gap, but also increases photo efficiency to manifold by providing conductive surface so photogenerated electrons and holes move apart and can be used for photoreduction of adsorbed CO<sub>2</sub> to methanol. The



**Scheme 2.** Plausible mechanism of  $\text{CO}_2$  reduction by  $\text{rGO@CuZnO@Fe}_3\text{O}_4$  **4**.

electrons and protons necessary for conversion of  $\text{CO}_2$  to methanol were derived from water splitting by positive holes present in the valence band of  $\text{ZnO}$ . This is worthy to mention that the reduction potential of  $\text{H}^+/\text{H}_2$  is ( $-0.41$  V vs NHE at pH-7) close enough to  $\text{CO}_2/\text{CH}_3\text{OH}$  ( $-0.38$  V vs NHE at pH 7); hence we observed hydrogen as a byproduct along with the desired methanol [3].

#### 4. Conclusions

We have developed novel magnetically separable core-shell structured reduced graphene oxide wrapped  $\text{rGO@CuZnO@Fe}_3\text{O}_4$  microspheres that have been used as photocatalyst for the photoreduction of  $\text{CO}_2$  to methanol under visible light irradiation. Owing to the synergistic effect of reduced graphene oxide and  $\text{CuZnO@Fe}_3\text{O}_4$  in the  $\text{rGO@CuZnO@Fe}_3\text{O}_4$  composite, significantly higher photocatalytic efficiency as compared to  $\text{CuZnO@Fe}_3\text{O}_4$  as well as  $\text{GO@CuZnO@Fe}_3\text{O}_4$  microspheres was observed. The methanol yield using  $\text{CuZnO@Fe}_3\text{O}_4$ ,  $\text{GO@CuZnO@Fe}_3\text{O}_4$  and  $\text{rGO@CuZnO@Fe}_3\text{O}_4$  was determined to be 858, 1749 and  $2656 \mu\text{mol g}^{-1} \text{ cat}$ , respectively. After completion of the reaction, the developed catalyst was easily recovered from the reaction mixture by an external magnet. The recovered catalyst showed consistent activity at least for six cycles and provided methanol in almost similar yields. As compared to the literature known photocatalysts, the developed photocatalyst offers several advantages such as high methanol yield, no need of sacrificial donor, facile recovery and efficient recycling.

#### Acknowledgements

Authors are thankful to Director IIP for granting permission to publish these results. PK is thankful to CSIR New Delhi for providing research fellowship. PK is also thankful for Cefipra and Campus France for providing fellowship under Raman–Charpak scheme. CJ kindly acknowledge CSIR, New Delhi for providing technical HR under XII five year projects. Analytical department is kindly acknowledged for the analysis of samples. RB acknowledges financial support from the CNRS, Lille1 University and Hauts-de-France

region. The TEM and SEM facilities in Lille (France) are supported by the Conseil Régional du Nord–Pas de Calais, and the European Regional Development Fund (ERDF).

#### Appendix A. Supplementary data

Supplementary data associated with this article can be found, in the online version, at <http://dx.doi.org/10.1016/j.apcatb.2016.11.060>.

#### References

- [1] P.M. Cox, R.A. Betts, C.D. Jones, S.A. Spall, I.J. Totterdell, *Nature* **408** (2000) 184–187.
- [2] X. Xiaoding, J.A. Moulijn, *Energy Fuels* **10** (1996) 305–325.
- [3] K. Li, X. An, K.H. Park, M. Khraisheh, J. Tang, *Catal. Today* **224** (2014) 3–12.
- [4] S. Das, W.M.A. Wan Daud, *Renew. Sustain. Energy Rev.* **39** (2014) 765–805.
- [5] C. Song, *Catal. Today* **115** (2006) 2.
- [6] T. Sakakura, J.-C. Choi, H. Yasuda, *Chem. Rev.* **107** (2007) 2365–2387.
- [7] G. Liu, N. Hoivik, K. Wang, H. Jakobsen, *Sol. Energy Mater. Sol. Cells* **105** (2012) 53–68.
- [8] F. Fresno, R. Portela, S. Suarez, J.M. Coronado, *J. Mater. Chem. A* **2** (2014) 2863–2884.
- [9] S. Xie, Y. Wang, Q. Zhang, W. Fan, W. Deng, Y. Wang, *Chem. Commun.* **49** (2013) 2451–2453.
- [10] Q. Zhai, S. Xie, W. Fan, Q. Zhang, Y. Wang, W. Deng, Y. Wang, *Angew. Chem.* **125** (2013) 5888–5891.
- [11] W. Fan, Q. Zhang, Y. Wang, *Phys. Chem. Chem. Phys.* **15** (2013) 2632–2649.
- [12] P. Kumar, N.G. Naumov, R. Boukherroub, S.L. Jain, *Appl. Catal. A* **499** (2015) 32–38.
- [13] A. Yarahmadi, S. Sharifnia, *Dyes Pigm.* **107** (2014) 140–145.
- [14] M.F. Ehsan, T. He, *Appl. Catal. B* **166–167** (2015) 345–352.
- [15] D. Wu, F. Zhang, H. Liang, X. Feng, *Chem. Soc. Rev.* **41** (2012) 6160–6177.
- [16] K.R. Ratinac, W. Yang, J.J. Gooding, P. Thordarson, F. Braet, *Electroanalysis* **23** (2011) 803–826.
- [17] S. Bai, X. Shen, *RSC Adv.* **2** (2012) 64–98.
- [18] H.-C. Hsu, I. Shown, H.-Y. Wei, Y.-C. Chang, H.-Y. Du, Y.-G. Lin, C.-A. Tseng, C.-H. Wang, L.-C. Chen, Y.-C. Lin, K.-H. Chen, *Nanoscale* **5** (2013) 262–268.
- [19] Y.T. Liang, B.K. Vijayan, K.A. Gray, M.C. Hersam, *Nano Lett.* **11** (2011) 2865–2870.
- [20] Y.T. Liang, B.K. Vijayan, O. Lyandres, K.A. Gray, M.C. Hersam, *J. Phys. Chem. Lett.* **3** (2012) 1760–1765.
- [21] M. Xing, F. Shen, B. Qiu, J. Zhang, *Sci. Rep.* **4** (2014) 6341.
- [22] L.-L. Tan, W.-J. Ong, S.-P. Chai, A.R. Mohamed, *Appl. Catal. B* **166–167** (2015) 251–259.
- [23] L. Zhang, N. Li, H. Jiu, G. Qi, Y. Huang, *Ceram. Int.* **41** (2015) 6256–6262.

[24] I. Shown, H.-C. Hsu, Y.-C. Chang, C.-H. Lin, P.K. Roy, A. Ganguly, C.-H. Wang, J.-K. Chang, C.-I. Wu, L.-C. Chen, K.-H. Chen, *Nano Lett.* 14 (2014) 6097–6103.

[25] X. An, K. Li, J. Tang, *ChemSusChem* 7 (2014) 1086–1093.

[26] P. Kumar, B. Sain, S.L. Jain, *J. Mater. Chem. A* 2 (2014) 11246–11253.

[27] P. Kumar, A. Kumar, B. Sreedhar, B. Sain, S.S. Ray, S.L. Jain, *Chem. Eur. J.* 20 (2014) 6154–6161.

[28] P. Kumar, H.P. Mungse, O.P. Khatri, S.L. Jain, *RSC Adv.* 5 (2015) 54929–54935.

[29] P. Kumar, A. Bansiwal, N. Labhsetwar, S.L. Jain, *Green Chem.* 17 (2015) 1605–1609.

[30] P. Kumar, H.P. Mungse, S. Cordier, R. Boukherroub, O.P. Khatri, S.L. Jain, *Carbon* 94 (2015) 91–100.

[31] W.S. Hummers, R.E. Offeman, *J. Am. Chem. Soc.* 80 (1958) 1339.

[32] H. Deng, X.L. Li, Q. Peng, X. Wang, J.P. Chen, Y.D. Li, *Angew. Chem. Int. Ed.* 44 (2005) 2782.

[33] K.-H. Choi, W.-S. Chae, E.-M. Kim, J.-H. Jun, J.-H. Jung, Y.-R. Kim, J.S. Jung, *IEEE trans. Magn.* 47 (2011) 3369–3372.

[34] X. Yu, J. Wan, Y. Shan, K. Chen, X. Han, *Chem. Mater.* 21 (2009) 4892–4898.

[35] J.S. Lee, K.H. You, C.B. Park, *Adv. Mater.* 24 (2012) 1084–1088.

[36] T. Xu, L. Zhang, H. Cheng, Y. Zhu, *Appl. Catal. B* 101 (2011) 382–387.

[37] I. Chamritski, G. Burns, *J. Phys. Chem. B* 109 (2005) 4965–4968.

[38] R. Wang, G. Xu, P. Jin, *Phys. Rev. B* 69 (2004) 113303.

[39] W.F.J. Fontijn, P.J. van der Zaag, M.A.C. Devillers, V.A.M. Brabers, R. Metselaar, *Phys. Rev. B* 56 (1997) 5432.

[40] W.F.J. Fontijn, P.J. van der Zaag, L.F. Feiner, R. Metselaar, M.A.C. Devillers, *J. Appl. Phys.* 85 (1999) 5100–5105.

[41] K.J. Kim, H.S. Lee, M.H. Lee, S.H. Lee, *J. Appl. Phys.* 91 (2002) 9974–9977.

[42] X. Wei, T. Xie, L. Peng, W. Fu, J. Chen, Q. Gao, G. Hong, D. Wang, *J. Phys. Chem. C* 115 (2011) 8637–8642.

[43] A. Janotti, C.G. Van de Walle, *Rep. Prog. Phys.* 72 (2009) 126501.

[44] J.-Y. Chen, T.-M. Wong, C.W. Chang, C.-Y. Dong, Y.-F. Chen, *Nat. Nanotechnol.* 9 (2014) 845–850.

[45] Y. Yan, M.M. Al-Jassim, S.H. We, *Appl. Phys. Lett.* 89 (2006) 181912.

[46] A. Cetin, R. Kibar, M. Ayvacik, N. Can, C. Buchal, P.D. Townsend, A.L. Stepanov, T. Karah, S. Selvi, *Nucl. Instrum. Methods Phys. Res. B* 249 (2006) 474–477.

[47] A.B. Djurisic, Y.H. Leung, K.H. Tam, Y.F. Hsu, L. Ding, W.K. Ge, C. Zhong, K.S. Wong, W.K. Chan, H.L. Tam, K.W. Cheah, W.M. Kwok, D.L. Phillips, *Nanotechnology* 18 (2007) 095702.

[48] L.J. Brillson, Y. Dong, F. Tuomisto, B.G. Svensson, A.Y. Kuznetsov, D. Doutt, H.L. Mosbacher, G. Cantwell, J. Zhang, J.J. Song, Z.-Q. Fang, D.C. Look, *Phys. Stat. Sol. C* 9 (2012) 1566–1569.

[49] H.A. Ahn, Y.Y. Kim, D.C. Kim, S.K. Mohanta, H.K. Cho, *J. Appl. Phys.* 105 (2009) 013502.

[50] X. Liu, X. Wu, H. Cao, R.P.H. Chang, *J. Appl. Phys.* 95 (2004) 3141.

[51] R.B.M. Cross, M.M.D. Souza, E.M.S. Narayanan, *Nanotechnology* 16 (2005) 2188.

[52] Z. Luo, P.M. Vora, E.J. Mele, A.T.C. Johnson, J.M. Kikkawa, *Appl. Phys. Lett.* 94 (2009) 111909.

[53] G. Eda, C. Mattevi, H. Yamaguchi, H. Kim, M. Chhowalla, *J. Phys. Chem. C* 113 (2009) 15768.

[54] M. Fu, Y. Li, S. Wu, P. Lu, J. Liu, F. Dong, *Appl. Surf. Sci.* 258 (2011) 1587–1591.

[55] R. Mohan, K. Krishnamoorthy, S.-J. Kim, *Solid State Commun.* 152 (2012) 375–380.

## Further reading

[56] E.M.P. Steinmiller, K.S. Choi, *Proc. Natl. Acad. Sci.* 106 (2009) 20633.